Supplementary Information for "A global increase in nearshore tropical cyclone intensification" by Balaguru, K., et al.

Supplementary text 1

While we broadly attributed changes in VWS to various processes based on SWM experiments in the main text, here we conduct a more detailed examination of those results and mechanisms. Figs. 4c-4e depict the decomposition of the SWM response (Fig. 4b) into three components: the change caused by anomalous diabatic heating (Fig. 4c), the evolving basic states (Fig. 4d), and the anomalous transient forcing (Fig. 4e). The similarity between Fig. 4b and Fig. 4c across the Western Hemisphere suggests that much of the shear response along the US coast and Mexican west coast is linked to changes in diabatic heating forced by anthropogenic warming (Supplementary Fig. 9a). Previously[1], it was proposed that the meridional dipole structure of shear response over the Central and North America is mainly excited by enhanced heating over the tropical eastern Pacific, with the secondary contribution arising from the anomalous diabatic cooling over the tropical North Atlantic (Supplementary fig. 9a). Circulation responses at different levels are largely consistent with Gill model's solution [2]. Furthermore, the projected changes in tropical heating are primarily shaped by the spatial pattern of future SST warming [3, 4, 5].

An altered zonal mean basic state is acting to decrease the VWS over Northeast Asia and the North Indian Ocean, while simultaneously causing a slight increase in shear near 40°N over North America (Fig. 4d). In accordance with the anomalous cyclone centered near the Tibetan Plateau, the westerly jet near Korea and Japan, as well as the the upper-level easterlies on the southern side of the Asian monsoon anticyclone both weaken (Supplementary fig. 10). Meanwhile, anomalous anticyclones above Hawaii and the tropical-subtropical North Atlantic result in a slight enhancement of extratropical westerlies over the northern US (Supplementary fig. 10). These upper-level circulation changes are consistent with the observed reductions in VWS over Northeast Asia and the North Indian Ocean, as well as the slight enhancement of shear near 40°N over North America (Fig. 4d). Upon closer examination, it is observed that the changes in basic states cause an overall decline in stationary wave circulations, especially south of 40°N (Supplementary fig. 10). This outcome aligns with the slowdown of tropical convective circulations that occur in a warmer climate [6, 7]. The coupling between vertical motion and rotational winds occurs through Sverdrup balance [8, 9]. Alternatively, the upper tropospheric vorticity can be altered by the divergent winds through vortex stretching and vorticity advection, and one may interpret convectively forced upper-level divergence as a source for Rossby waves [10]. Decreased convective mass fluxes in the tropics, along with the slower overturning circulation, can be primarily attributed to the heightened static stability of the tropical-subtropical troposphere (Supplementary Fig. 9b), which is a robust consequence of the quasi-moist adiabatic adjustment to surface warming [11, 12, 13]. From the perspective of energy balance, the strength of the atmospheric overturning circulation must decrease as the climate warms because precipitation changes are constrained by small variations in radiative fluxes and cannot increase as fast as lower tropospheric moisture content [14, 6, 7]. An additional sensitivity experiment was conducted to further investigate the impact of increased warming in the upper troposphere on shear changes. The experiment only retains the enhanced upper-level warming (not shown). Interestingly, as compared to Figure 4d, the spatial pattern of VWS response over the Northern Hemisphere remains largely unchanged (not shown). Thus, we conclude that the enhanced static stability plays a crucial role in reducing the VWS across Northeast Asia and the North Indian Ocean.

Climate change-induced anomalous heating has contrasting effects on the VWS over different regions. It contributes to a decrease in VWS near Taiwan and the southeastern coast of China, but tends to strengthen VWS over northeast Asia and the northern Indian Ocean (Fig. 4c). Further investigation reveals that the meridional tripole-like pattern of VWS change over the Asian continent and the western North Pacific (Fig. 4c) is mainly driven by the formation of a heat-induced stationary baroclinic Rossby wave (Supplementary fig. 11). The circulation response exhibits a phase reversal in its vertical structure (Supplementary fig. 11) and is likely reinforced by intensified heat sources over the western North Pacific and the Indian sub-continent (Supplementary fig. 9a)[15], consistent with the projected increases of monsoon precipitation over these regions [16, 17, 18, 19, 20]. At 200 hPa, the anomalous high contributes to an acceleration of the jet on its northern and southern flanks (Supplementary fig. 11a), which causes the VWS to increase between 40°N and 50°N and above the northern Indian Ocean (Figs. 4b and 4c). On the other hand, the strengthened easterly wind between 20°N and 30°N (Supplementary fig. 11a) counteracts the weak westerlies above Taiwan and the coastal region of southeastern China, reducing the shear over these regions (Fig. 4c).

References

[1] Balaguru, K. *et al.* Increased us coastal hurricane risk under climate change. *Science Advances* **9** (2023).

[2] Gill, A. E. Some simple solutions for heat-induced tropical circulation. *Quarterly Journal of the Royal Meteorological Society* **106**, 447–462 (1980).

[3] Xie, S.-P. *et al.* Global warming pattern formation: Sea surface temperature and rainfall. *Journal of Climate* **23**, 966–986 (2010).

[4] Chadwick, R., Good, P., Andrews, T. & Martin, G. Surface warming patterns drive tropical rainfall pattern responses to co2 forcing on all timescales. *Geophysical Research Letters* **41**, 610–615 (2014).

[5] Kent, C., Chadwick, R. & Rowell, D. P. Understanding uncertainties in future projections of seasonal tropical precipitation. *Journal of Climate* **28**, 4390–4413 (2015).

[6] Held, I. M. & Soden, B. J. Robust responses of the hydrological cycle to global warming. *Journal of climate* **19**, 5686–5699 (2006).

[7] Vecchi, G. A. & Soden, B. J. Global warming and the weakening of the tropical circulation. *Journal of Climate* **20**, 4316–4340 (2007).

[8] Wills, R. C., White, R. H. & Levine, X. J. Northern hemisphere stationary waves in a changing climate. *Current climate change reports* **5**, 372–389 (2019).

[9] Chen, T.-C. Maintenance of summer monsoon circulations: A planetary-scale perspective. *Journal of climate* **16**, 2022–2037 (2003).

[10] Sardeshmukh, P. D. & Hoskins, B. J. The generation of global rotational flow by steady idealized tropical divergence. *Journal of the Atmospheric Sciences* **45**, 1228–1251 (1988).

[11] Manabe, S. & Wetherald, R. T. The effects of doubling the co 2 concentration on the climate of a general circulation model. *Journal of Atmospheric Sciences* **32**, 3–15 (1975).

[12] Knutson, T. R. & Manabe, S. Time-mean response over the tropical pacific to increased c02 in a coupled ocean-atmosphere model. *Journal of Climate* **8**, 2181–2199 (1995).

[13] Held, I. M. Large-scale dynamics and global warming. *Bulletin of the American Meteorological Society* **74**, 228–242 (1993).

[14] Betts, A. K. Climate-convection feedbacks: Some further issues. *Climatic Change* **39**, 35 (1998).

[15] Ting, M. Maintenance of northern summer stationary waves in a gcm. *Journal of the atmospheric sciences* **51**, 3286–3308 (1994).

[16] Sun, Y. & Ding, Y. A projection of future changes in summer precipitation and monsoon in east asia. *Science China Earth Sciences* **53**, 284–300 (2010).

[17] Seo, K.-H., Ok, J., Son, J.-H. & Cha, D.-H. Assessing future changes in the east asian summer monsoon using cmip5 coupled models. *Journal of climate* **26**, 7662–7675 (2013).

[18] He, C., Li, T. & Zhou, W. Drier north american monsoon in contrast to asian–african monsoon under global warming. *Journal of Climate* **33**, 9801–9816 (2020).

[19] Chen, Z. *et al.* Global land monsoon precipitation changes in cmip6 projections. *Geophysical Research Letters* **47**, e2019GL086902 (2020).

[20] Wang, B., Jin, C. & Liu, J. Understanding future change of global monsoons projected by cmip6 models. *Journal of Climate* **33**, 6471–6489 (2020).

[21] Kossin, J. P., Knapp, K. R., Olander, T. L. & Velden, C. S. Global increase in major tropical cyclone exceedance probability over the past four decades. *Proceedings of the National Academy of Sciences* **117**, 11975–11980 (2020).

[22] Rayner, N. *et al.* Global analyses of sea surface temperature, sea ice, and night marine air temperature since the late nineteenth century. *Journal of Geophysical Research: Atmospheres* **108** (2003).

[23] Kanamitsu, M. *et al.* Ncep–doe amip-ii reanalysis (r-2). *Bulletin of the American Meteorological Society* **83**, 1631–1644 (2002).

[24] Hersbach, H. *et al.* The era5 global reanalysis. *Quarterly Journal of the Royal Meteorological Society* **146**, 1999–2049 (2020).

[25] Haarsma, R. J. *et al.* High resolution model intercomparison project (highresmip v1. 0) for cmip6. *Geoscientific Model Development* **9**, 4185–4208 (2016).

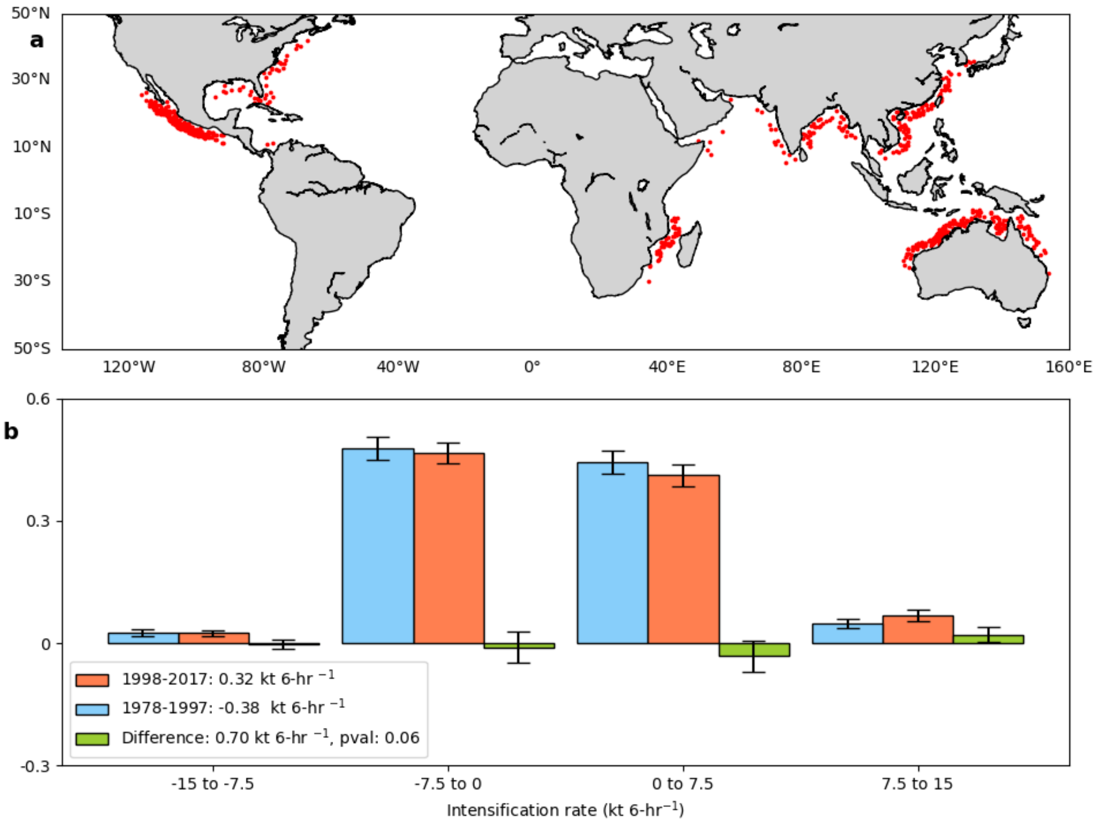

Supplementary figure 1: Observed changes in TC intensification based on ADT-HURSAT (1978-2017) a) Nearshore TC track locations used in this analysis. b) Probability distributions of 24-hr intensification rates for the initial period (1978-1997) in blue, later period (1998-2017) in orange and the difference in green. The mean TC intensification rates for the two periods and the mean difference, including the p-value, are shown in the figure legend. A Student's t-test for difference of means is used to ascertain statistical significance. The error bars have been estimated using the Monte Carlo method of repeated random sampling. Note that the data have been sub-sampled to ensure that distributions of storm state are statistically similar for the two periods (see 'Methods'). TC track data are based on ADT-HURSAT [21].

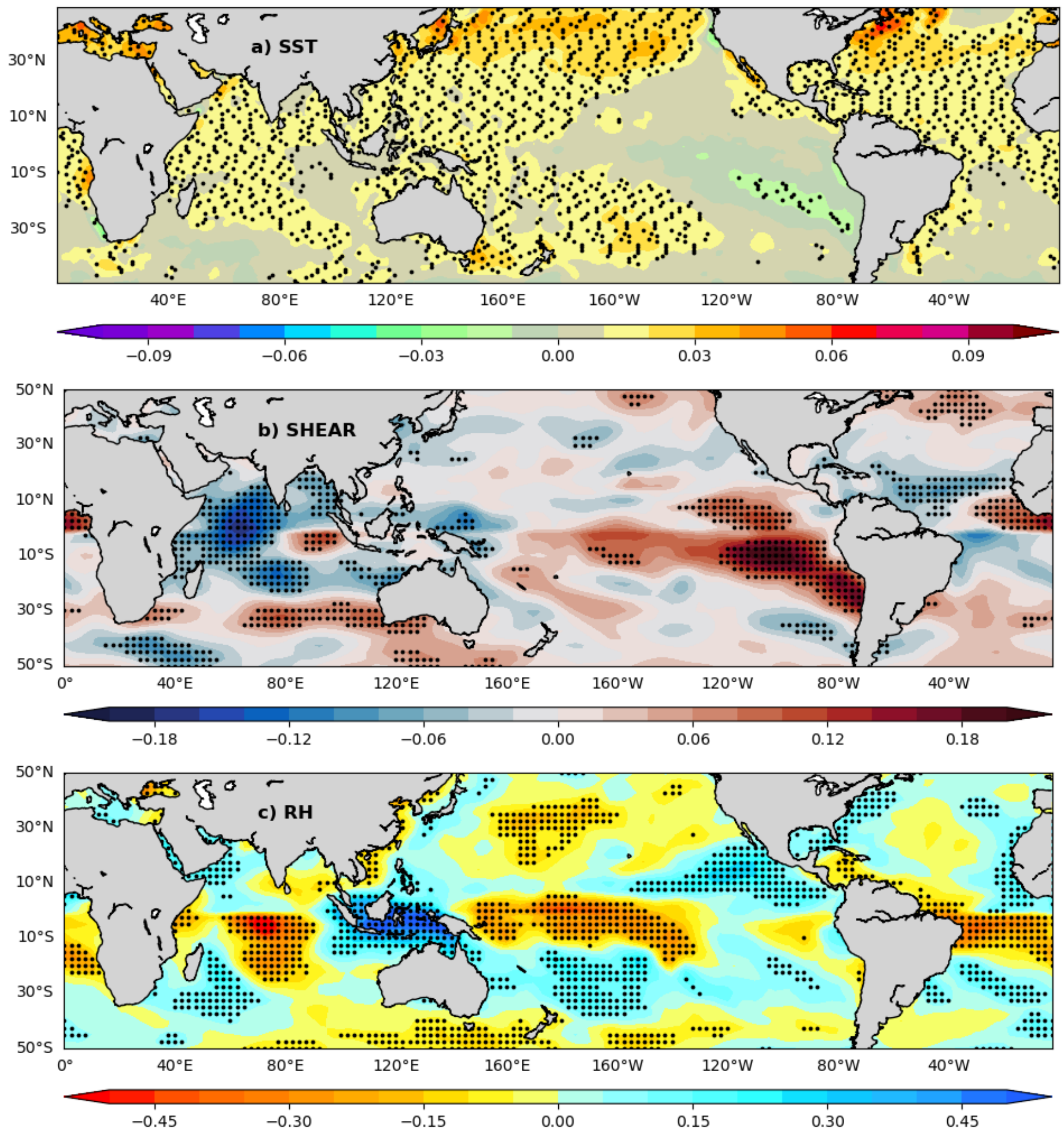

Supplementary figure 2: Observed trends in TC environment (1979-2020) Trends in a) SST (°C year^{-1}), b) VWS (m s^{-1} year^{-1}) and c) RH (% year^{-1}) for the 42-year period 1979-2020. The parameters have been averaged over the months of June-October in the Northern Hemisphere and December-April in the Southern Hemisphere. While the SST data are from the UK Met Office's Hadley Center [22], atmospheric winds and humidity are from NCEP-DOE II reanalysis [23]. Stippling indicates that trends are statistically significant at the 5% level.

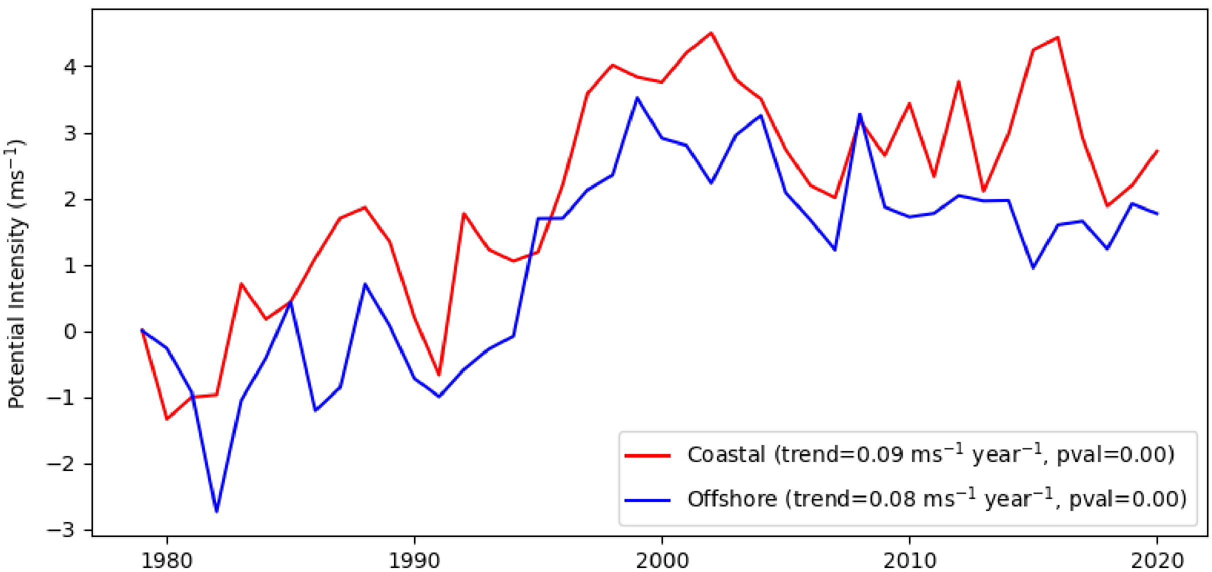

Supplementary figure 3: Observed trends in Potential Intensity(1979-2020) Nearshore and Offshore trends in thermodynamic Potential Intensity (ms^{-1} year^{-1}) for the 42-year period 1979-2020. Potential Intensity has been averaged over the months of June-October in the Northern Hemisphere and December-April in the Southern Hemisphere. Here, Potential Intensity is computed using SST data from the UK Met Office's Hadley Center [22], atmospheric winds, humidity and sea-level pressure from NCEP-DOE II reanalysis [23]. The trend values and p-values for statistical significance are provided in the legend. Consistent with SST, trends in Potential Intensity for nearshore and offshore locations are similar.

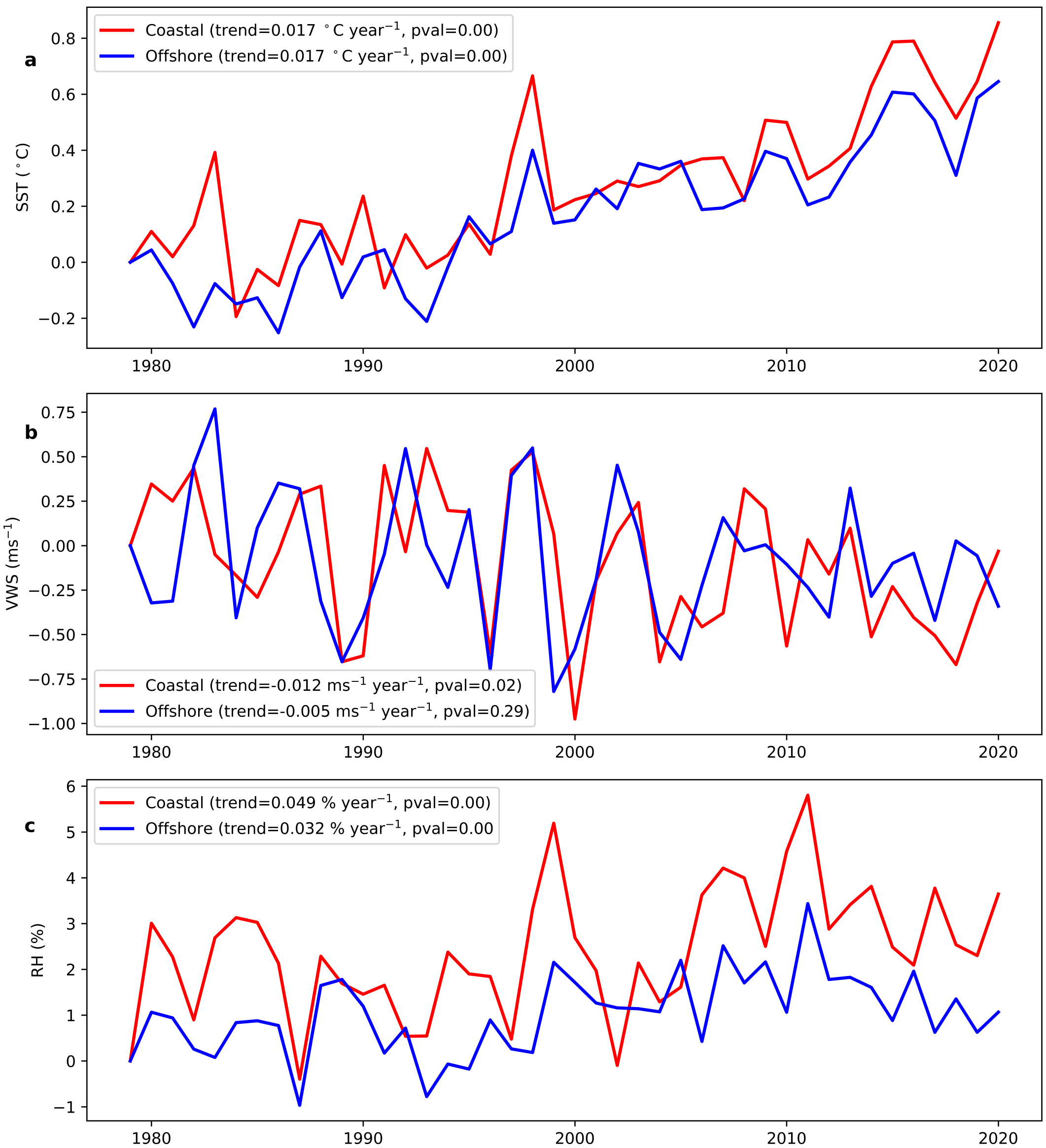

Supplementary figure 4: Observed trends in TC environment based on ERA5 (1979-2020) 42-year trends in a) SST (°C year^{-1}), b) Vertical Wind Shear (ms^{-1} year^{-1}), and c) Relative Humidity at 600 hPa (% year^{-1}). The parameters have been averaged over the months of June-October in the Northern Hemisphere and December-April in the Southern Hemisphere. The trend values and the p-values for statistical significance, based on the Student's t-test, are shown in the figure legends. For further details regarding the domains used for averaging, please see 'Methods'. Trends are based on ERA5 atmospheric reanalysis [24].

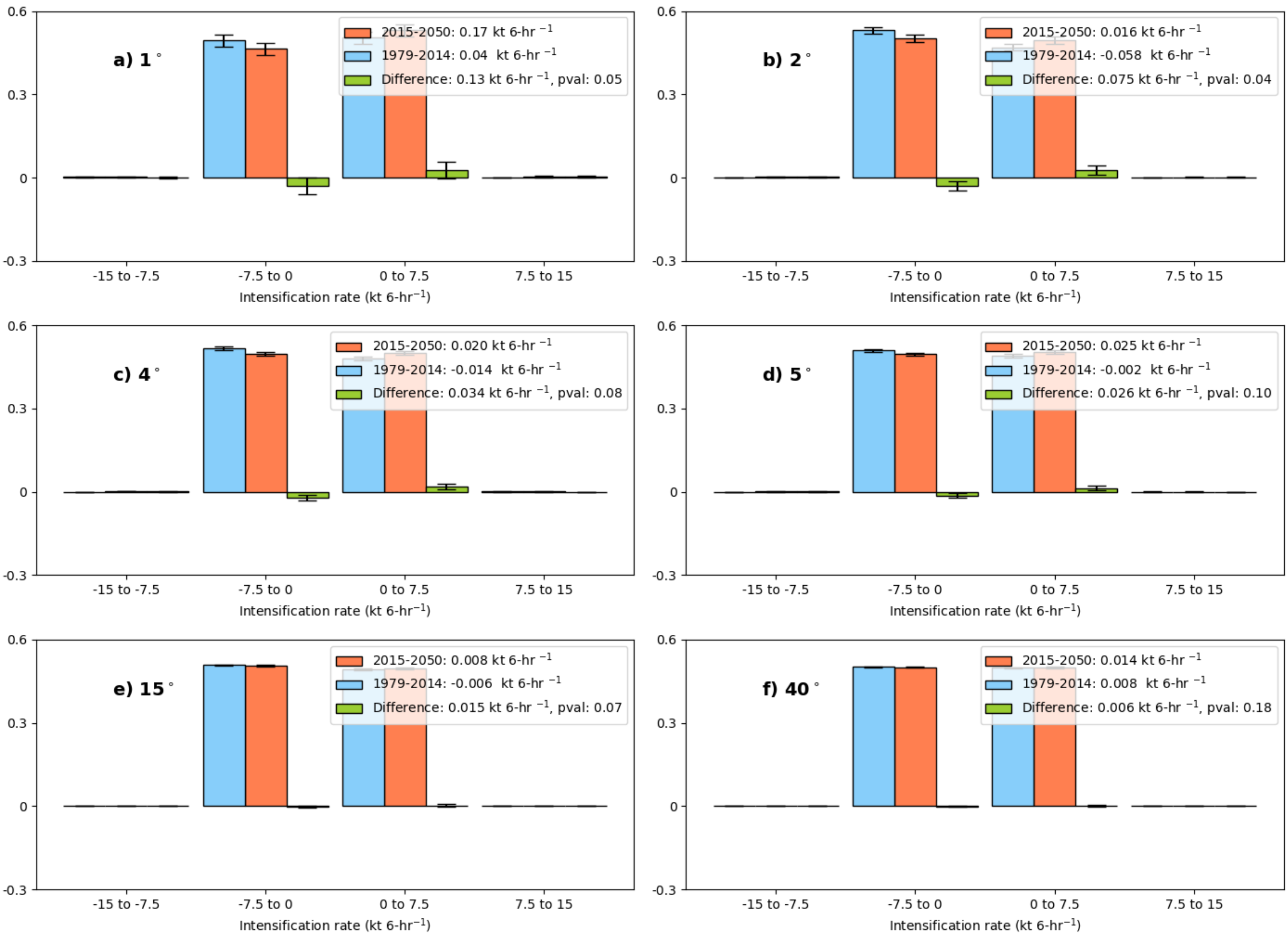

Supplementary figure 5: Sensitivity to the distance threshold Probability distributions of 24-hr intensification rates for the historical period (1979-2014) in blue, later period (2015-2050) in orange and the difference in green for various distance thresholds. The mean TC intensification rates for the two periods and the mean difference, including the p-value, are shown in the figure legend. Also shown in each figure is the corresponding distance threshold used. The error bars have been estimated using the Monte Carlo method of repeated random sampling. Note that the data have been sub-sampled to ensure that distributions of storm state are statistically similar for the two periods (see 'Methods'). TC track data are obtained from 5 fully coupled climate models belonging to HighResMIP [25]. See 'Methods' for more details regarding the various models and simulations used.

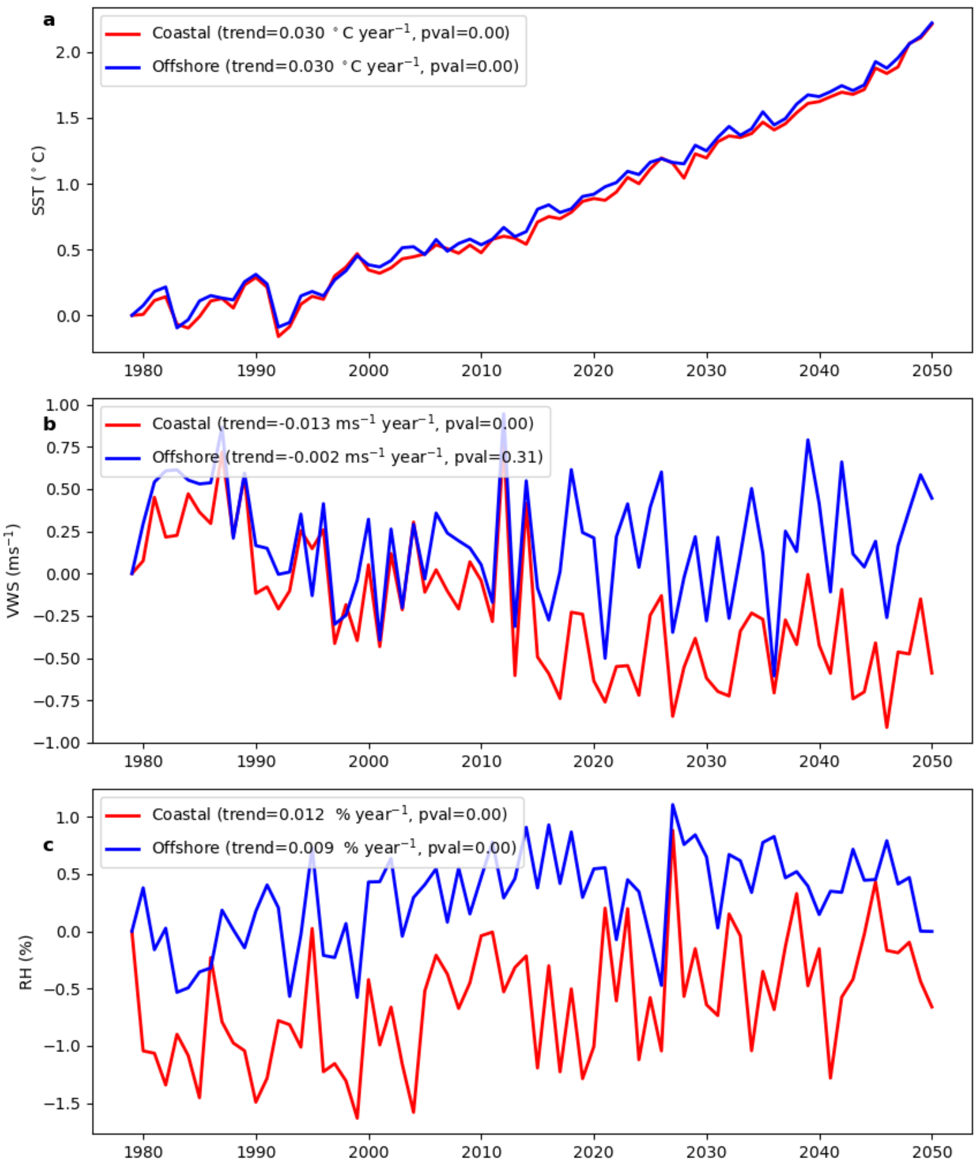

Supplementary figure 6: Projected trends in TC environment based on HighResMIP (1979-2050) Multi-model ensemble mean trends in a) SST (°C year^{-1}), b) VWS (ms^{-1} year^{-1}) and c) RH (% year^{-1}) for the 72-year period 1979-2050 based on 5 fully-coupled HighResMIP models. The parameters have been averaged over the months of June-October in the Northern Hemisphere and December-April in the Southern Hemisphere. The trend values and the p-values for statistical significance, based on the Student's t-test, are shown in the figure legends. The future climate corresponds to the SSP585 emissions scenario. For more details regarding the various models used, see 'Methods'.

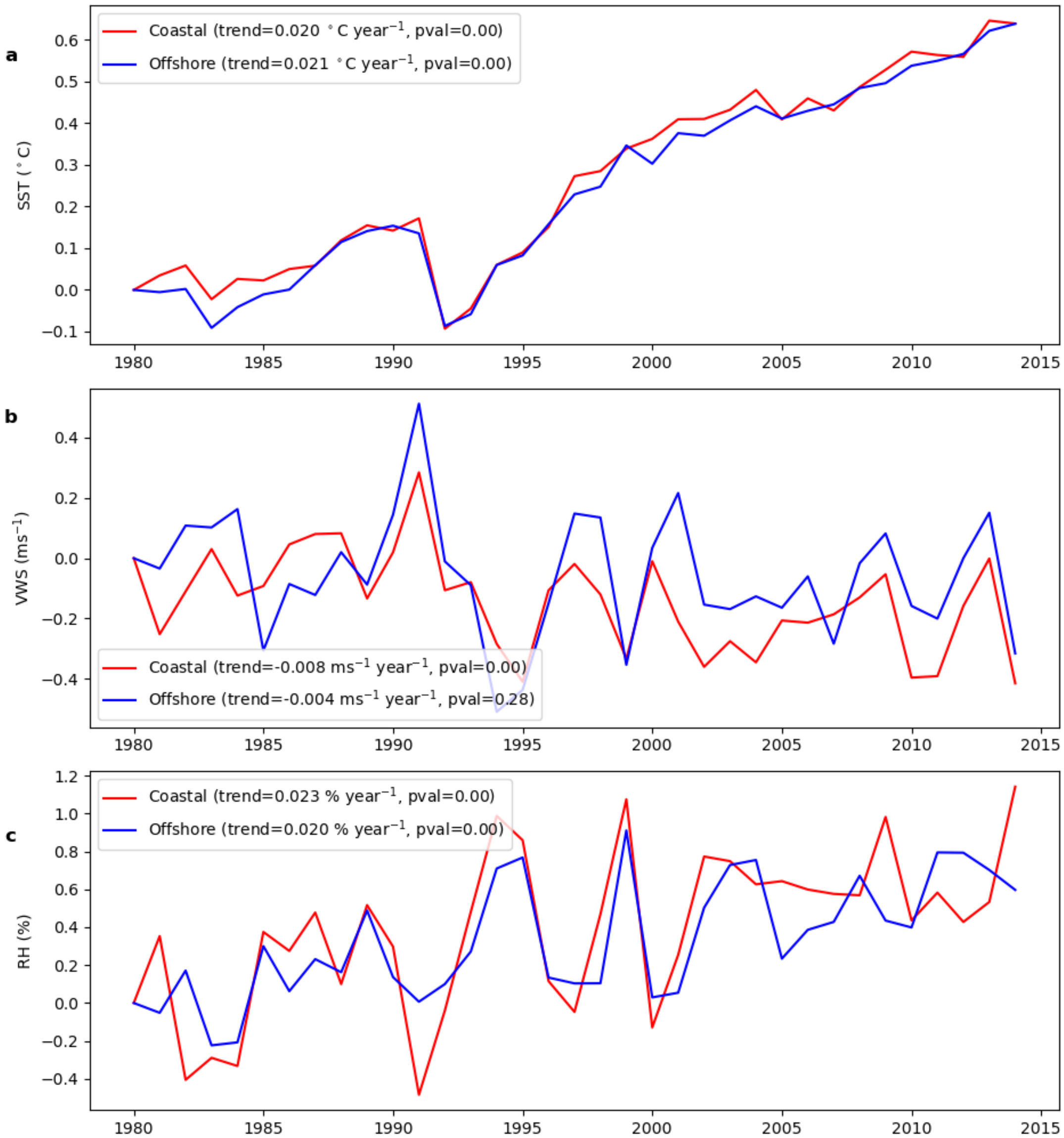

Supplementary figure 7: Simulated trends in TC environment based on CMIP6 (1980-2014) Multi-model ensemble mean trends in a) SST (°C year^{-1}), b) VWS (ms^{-1} year^{-1}) and c) RH (% year^{-1}) for the 35-year period 1980-2014 based on 15 CMIP6 models. The parameters have been averaged over the months of June-October in the Northern Hemisphere and December-April in the Southern Hemisphere. The trend values and the p-values for statistical significance, based on the Student's t-test, are shown in the figure legends. For more details regarding the various models used, see 'Methods'.

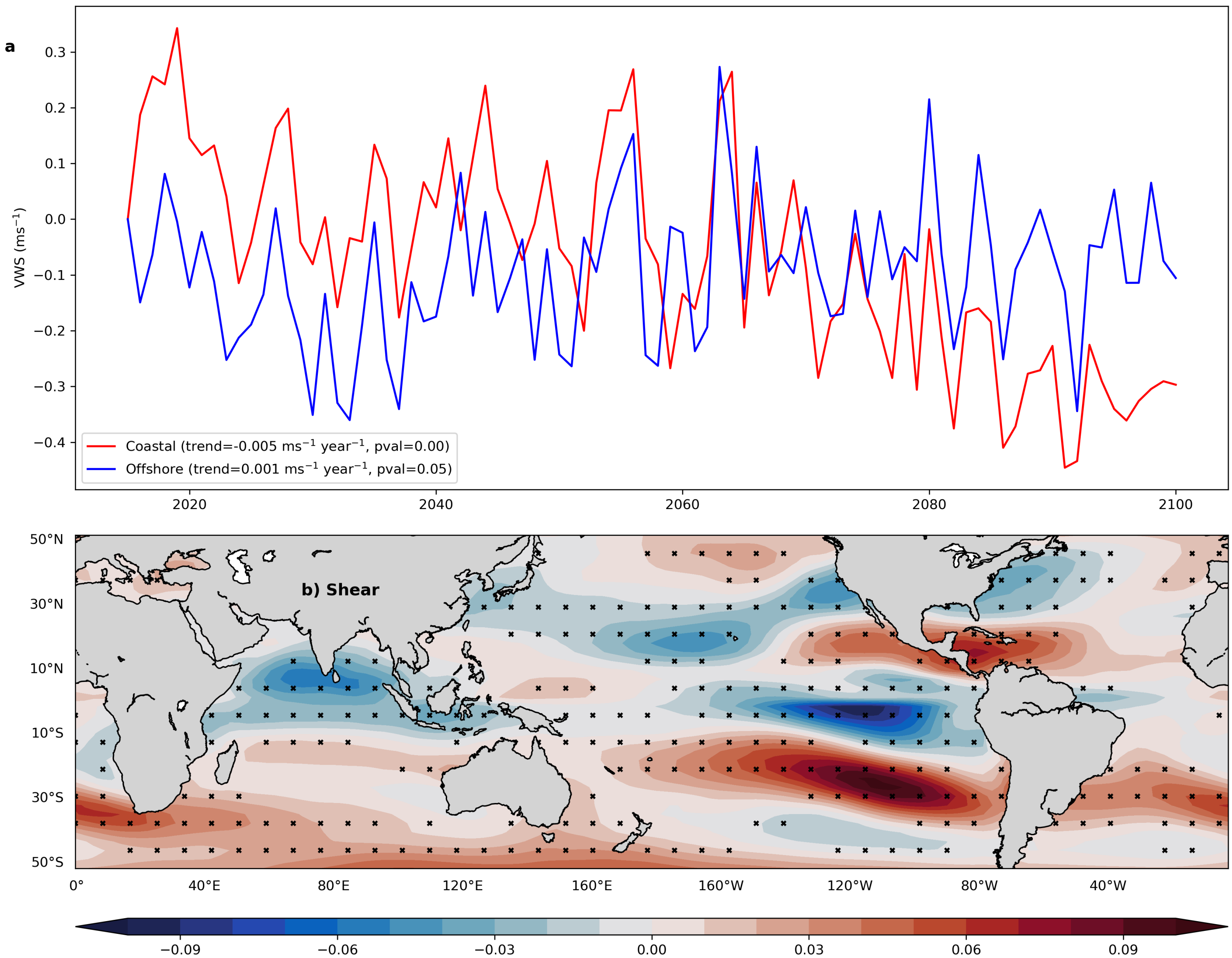

Supplementary figure 8: Projected long-term trends in VWS based on CMIP6 (2015-2100) Multi-model ensemble mean trends in VWS (ms^{-1} year^{-1}) for the 86-year period 2015-2100 based on 15 fully-coupled CMIP6 models. The parameters have been averaged over the months of June-October in the Northern Hemisphere and December-April in the Southern Hemisphere. In panel a, for trends averaged over the nearshore and offshore regions, the trend values and the p-values for statistical significance based on the Student's t-test are shown in the figure legend. The future climate corresponds to the SSP585 emissions scenario. For more details regarding the various models used, see 'Methods'.

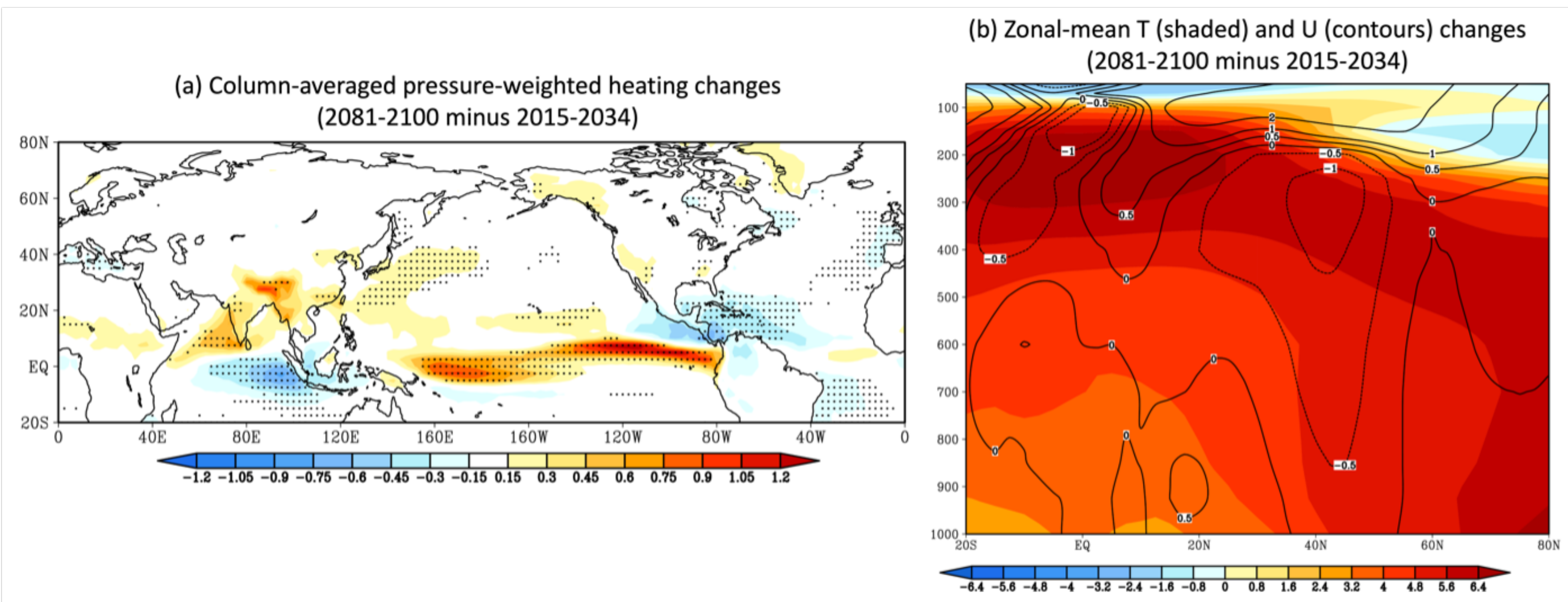

Supplementary figure 9: Projected changes in global diabatic heating and zonal-mean basic states (2015-2100) a) Projected changes in column-averaged pressure-weighted diabatic heating (K day^{-1}) by 15 CMIP6 models. Stippling indicates locations where the ensemble-mean changes are statistically significant at the 95% confidence level. (b) Zonal-mean zonal wind (m s^{-1}) and temperature (K) responses to climate change in 15 CMIP6 models. 'Change' indicates the difference between the mean over the late 21st period (2081-2100) and the near future (2015-2034) epoch.

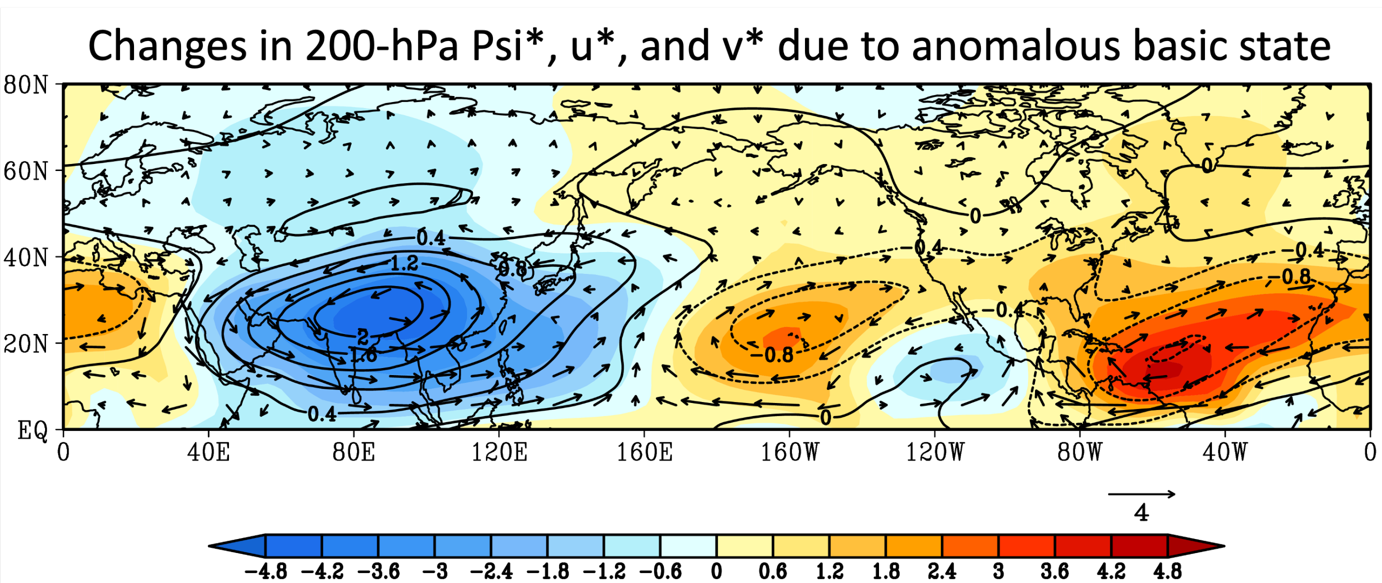

Supplementary figure 10: Atmospheric circulation response to basic state changes Contribution from the anomalous zonal mean basic state to changes in the 200-hPa eddy streamfunction (shaded, 10^6 m^2 s^{-1}) and winds (vector, m s^{-1}). 200-hPa eddy streamfunction in the CTRL experiment is represented by black contours (10^7 m^2 s^{-1}).

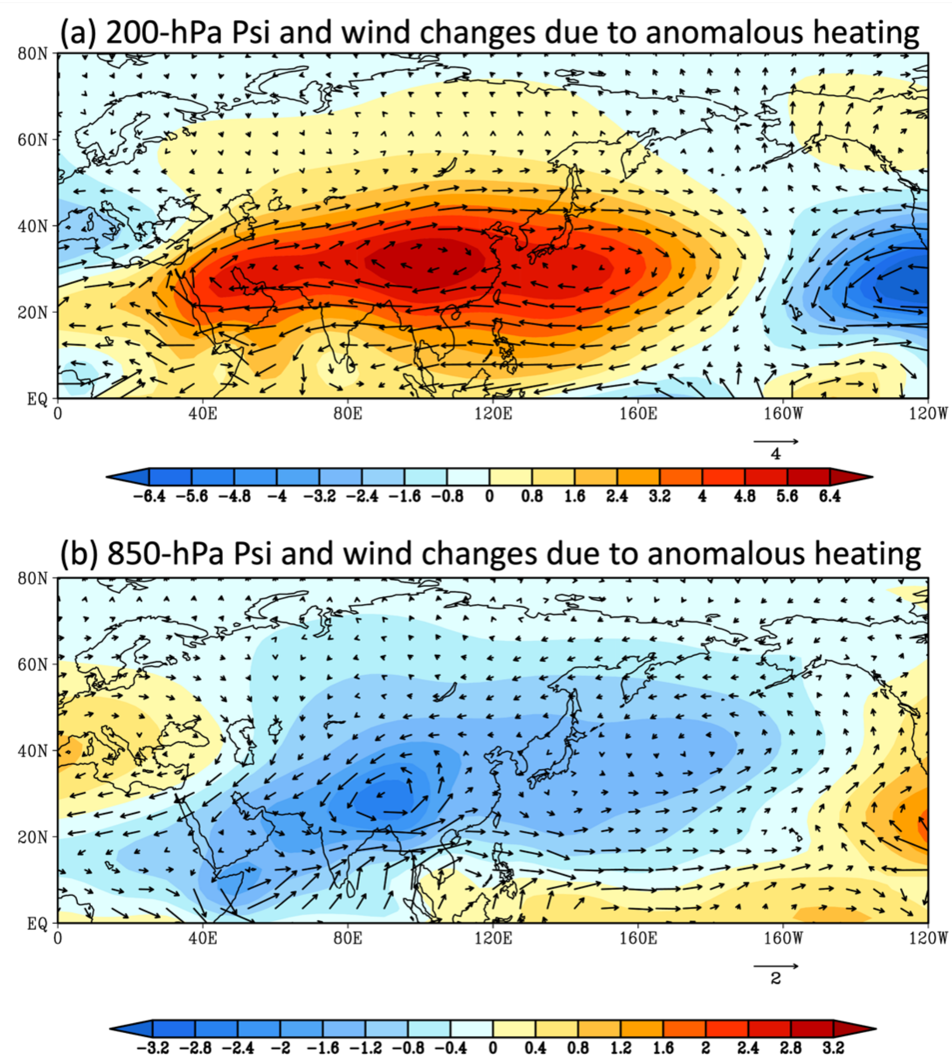

Supplementary figure 11: Atmospheric circulation response to heating changes a) Contribution from the anomalous heating to changes in the streamfunction (shaded, 10^6 m^2 s^{-1}) and winds (vector, m s-1) at 200 hPa. b) Same as (a), but at 850 hPa. These results are based on numerical experiments with the SWM. For further details regarding the configuration of the SWM and the various experiments, see 'Methods'.

Supplementary table 1: Observed trends in the TC environment for major coastlines (1979-2020) Observed trends in the nearshore and offshore TC environment for major coastlines of the world and for the 42-year period 1979-2020. For various coastlines, a distance of 3° within the coast is considered 'nearshore'. Parameters are averaged over June-October for the Northern Hemisphere, and from December-April for the Southern Hemisphere. Hadley SST and NCEP-DOE II reanalysis are used to compute the various parameters. The values in bold indicate trends that are statistically significant at the 95% level based on a Student's t-test.

	US East and Gulf coasts	**Mexican west coast**	**East Asian coast**	**South Asian coast**	**Southeast African coast**	**Australian coast**
Nearshore SST trend (°C year^{-1})	**0.020**	**0.012**	**0.018**	**0.011**	**0.008**	**0.012**
Offshore SST trend (°C year^{-1})	**0.018**	**0.009**	**0.017**	**0.012**	**0.011**	**0.009**
Nearshore VWS trend (ms^{-1} year^{-1})	-0.017	-0.013	**-0.027**	**-0.037**	**-0.021**	-0.013
Offshore VWS trend (ms^{-1} year^{-1})	**-0.016**	0.004	-0.008	**-0.065**	**-0.031**	-0.001
Nearshore RH trend (% year^{-1})	**0.100**	**0.069**	**-0.062**	0.049	0.015	**0.137**
Offshore RH trend (% year^{-1})	0.004	**0.085**	-0.024	0.031	**-0.030**	**0.037**

Supplementary table 2: List of various experiments conducted with the Stationary Wave Model (SWM) Zonal-mean basic states, diabatic heating, and transient forcings are obtained from either the CMIP6 SSP585 runs during two time periods: the near future (2015-2034) or the late 21^{st} century (2081-2100). Each experiment is integrated for 100 days, and the average from days 31 to 100 is shown. Zonal-mean basic states and diabatic heating are calculated based on monthly-mean outputs from 15 CMIP6 models, but transient momentum forcing is estimated from daily three-dimensional winds simulated by 13 CMIP6 models. Daily outputs are unavailable from E3SM-1-1 and CNRM-ESM2-1.

	CTRL	**Future**	**CTRL+ΔBS**	**CTRL+ΔDH**	**CTRL+ΔTranF**
Basic states (BS)	**From 2015-2034**	**From 2081-2100**	**From 2081-2100**	**From 2015-2034**	**From 2015-2034**
Diabatic heating (DH)	**From 2015-2034**	**From 2081-2100**	**From 2015-2034**	**From 2081-2100**	**From 2015-2034**
Transient divergence and vorticity (TranF)	**From 2015-2034**	**From 2081-2100**	**From 2015-2034**	**From 2015-2034**	**From 2081-2100**